

This item is the archived peer-reviewed author-version of:

Third-order nonlinear optical properties and saturation of two-photon absorption in lead-free double perovskite nanocrystals under femtosecond excitation

Reference:

Mushtaq Aamir, Pradhan Bapi, Kushavah Dushyant, Zhang Yiyue, Wolf Mathias, Schrenker Nadine, Fron Eduard, Bals Sara, Hofkens Johan, Debroye Elke,-
Third-order nonlinear optical properties and saturation of two-photon absorption in lead-free double perovskite nanocrystals under femtosecond excitation
ACS Photonics - ISSN 2330-4022 - 8:11(2021), p. 3365-3374
Full text (Publisher's DOI): <https://doi.org/10.1021/ACSPHOTONICS.1C01351>
To cite this reference: <https://hdl.handle.net/10067/1842490151162165141>

Third-Order Nonlinear Optical Properties and Saturation of Two-Photon Absorption in Lead-Free Double Perovskite Nanocrystals under Femtosecond Excitation

Aamir Mushtaq^{§#}, Bapi Pradhan^{§#}, Dushyant Kushavah[§], Yiyue Zhang[§], Mathias Wolf[§],
Nadine Schrenker^α, Eduard Fron[§], Sara Bals^α, Johan Hofkens^{§,δ}, Elke Debroye[§], Suman
Kalyan Pal^{§*}

*§School of Basic Sciences and Advanced Material Research Center, Indian Institute of
Technology Mandi, Kamand 175005, H.P, India*

§Department of Chemistry, KU Leuven, Celestijnenlaan 200F, 3001 Heverlee, Belgium

δMax Planck Institute for Polymer Research, Ackermannweg 10, 55128 Mainz, Germany

*αElectron Microscopy for Materials Research, University of Antwerp, Groenenborgerlaan,
171, 2020 Antwerp, Belgium*

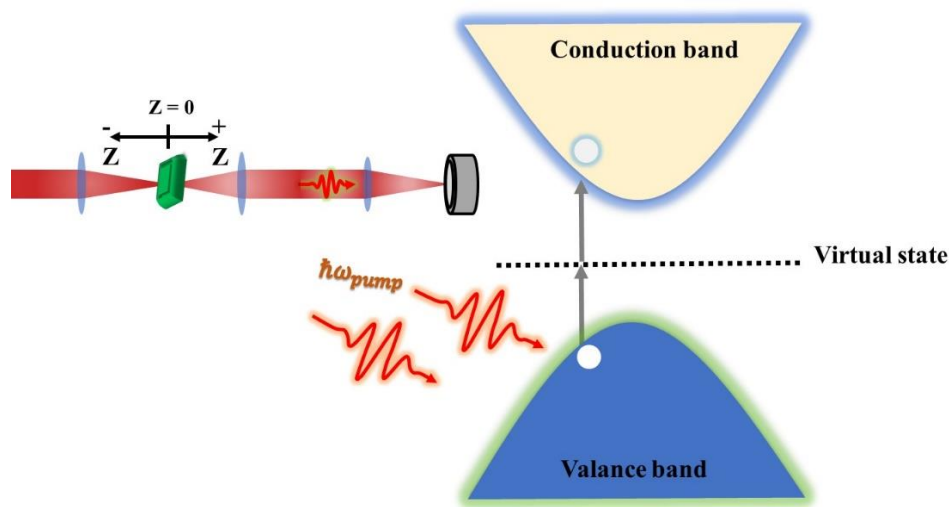
Abstract

Lead halide perovskites have been widely explored in the field of photovoltaics, light-emitting diodes and lasers due to their outstanding linear and nonlinear optical (NLO) properties. But, the presence of lead toxicity and low chemical stability remain serious concerns. Lead-free double perovskite with excellent optical properties and chemical stability could be an alternative. However, proper examination of the NLO properties of such a material is crucial to identify their utility for future nonlinear device applications. Herein, we have made use of femtosecond (fs) Z-scan technique to explore the NLO properties of Cs₂AgIn_{0.9}Bi_{0.1}Cl₆ nanocrystals (NCs). Our measurements suggest that under nonresonant fs excitation, perovskite NCs exhibit strong two-photon absorption (TPA). The observed saturation of TPA at high light intensities has been explained by a customized model. Furthermore, we have demonstrated a

change in the nonlinear refractive index of the NCs under varying input intensities. The strong TPA absorption of lead-free double perovskite NCs could be used for Kerr nonlinearity-based nonlinear applications such as optical shutters for picosecond lasers.

Keywords: Z-scan, TPA saturation, Double perovskite, Nonlinear optics, Nonlinear refractive index.

TOC



INTRODUCTION

Strong interaction of intense light with matter comes under the class of nonlinear optics which becomes extremely important for modern technologies. The nonlinear optical properties of a specific material play an important role in revealing light-matter interactions and ultrafast dynamics.^{1,2} Formation of new secondary optical fields and variation of phase and frequency instigated by polarization, made the NLO effect a keystone for the manipulation of photons in advanced technologies such as optical computation, information processing and storage, and telecommunication.³⁻⁶ The NLO effect has been identified in a series of materials including transition metal dichalcogenides (TMDCs),^{7,8} graphene,^{9,10} hexagonal boron nitride (h-BN)¹¹ and metal organic frameworks (MOFs).^{12,13} The materials possessing optical nonlinearities

find applications in optical switches, optical data storage^{14, 15} and lasers.¹⁶ Nowadays, switching of optical signals in optical communication is achieved through optical-to-electronic-to-optical (OEO) transmutation components. Operation of such photonic devices is based on the instantaneous Kerr effect which occurs when bound electronic charges of material are virtually excited by photons having energies less than the bandgap resulting in change in refractive index of the material.¹⁷ The Kerr effect in thin films is generally weak, and in that case direct single or multiphoton absorption process can bring the change in refractive index that is significantly larger than the change due to Kerr effect. In contrast, the linear electro-optic or Pockels effect (a second order process) where the change in refractive index varies linearly with the electric field (of laser beam) finds application in electro-optic modulators. However, due to intrinsic centrosymmetric structures, traditional perovskites (CsPbX_3 or MAPbX_3) are not useful for applications based on the Pockels effect.¹⁸ A recent report shows that germanium based perovskite (CsGeI_3) exhibits an electro-optic coefficient which is better than that of LiNbO_3 .¹⁹ It is worth mentioning that the optical Kerr effect is present in all centrosymmetric media, but the strength of this effect is weaker than the linear electro-optic effect. Furthermore, carrier induced third-order nonlinearities depend on carrier diffusion length and recombination of carriers in a material.

Metal halide perovskites (MHPs) exhibit remarkable optoelectronic properties like high absorption coefficients, long carrier diffusion lengths and high photoluminescence (PL) intensities.^{20, 21} Moderate exciton binding energies²² and tuneable bandgaps along with rich structural and chemical diversity of halide perovskites enable their application in varieties of photonic²³ and optoelectronic devices like lasers,^{24, 25} photodetectors, and LEDs.^{26, 27} According to recent reports, all inorganic CsPbBr_3 perovskite NCs possess a remarkable TPA cross-section ($\sim 10^5$ GM).^{28, 29} Moreover, the rich structural diversity of 2D hybrid organic-inorganic perovskites makes them useful for optics and optoelectronics applications.³⁰ Apart

from these, hybrid organic-inorganic metal halide perovskite ($\text{CH}_3\text{NH}_3\text{PbX}_3$, $\text{X} = \text{Br}, \text{Cl}, \text{I}$) NC films exhibit strong nonlinear optical properties in the mid-IR region.³¹ Ni-doped CsPbI_3 NCs have been shown to possess a strong TPA cross-section (10^4 GM) with a TPA coefficient and nonlinear refractive index of the order of 10^{-11} cm/W and $10^{-12} \text{ cm}^2/\text{W}$, respectively.³² Despite of these superior properties, lead toxicity and low chemical stability of these perovskites remain a concern which require the exploration of new lead-free perovskites to alleviate these issues.

Several methods have been adopted to replace lead from MHPs. Initially, tin (Sn) was used as substitute, however, Sn-based perovskites are extremely unstable under ambient conditions due to facile oxidation of Sn^{2+} to Sn^{4+} .³³⁻³⁵ Further, lead-free perovskites based on Bi^{3+} and Sb^{3+} possess an indirect bandgap.^{36, 37} Double perovskites with a general formula of $\text{A}_2\text{BB}^*\text{X}_6$ (where B and B^* are two size compatible cations, A is a monovalent cation and X is a halide), on the other hand, could prove to be a more stable alternative of conventional MHPs. The nonlinear optical properties of this class of perovskites still need to be explored in order to utilize them in nonlinear optical devices. In the present work, we explore third-order nonlinear optical properties of $\text{Cs}_2\text{AgIn}_{0.9}\text{Bi}_{0.1}\text{Cl}_6$ double perovskite NCs in the fs regime by exploiting open aperture (OA) and closed aperture (CA) Z-scan techniques.

EXPERIMENTAL METHODS

The Z-scan setup (Figure 1) used in this work has been previously described elsewhere.³⁸ In brief, a Ti:sapphire regenerative amplifier (Spitfire ace, Spectra Physics) seeded by an oscillator (Mai Tai SP, Spectra Physics) was used as a light source. A fraction of the laser output from the amplifier having a central wavelength 800 nm and a pulse width 57 fs was used for measurement. To record intensities of reference and sample signals, we split the beam into two parts with the help of a beam splitter (BS1). Then one beam finds its path to photodetector

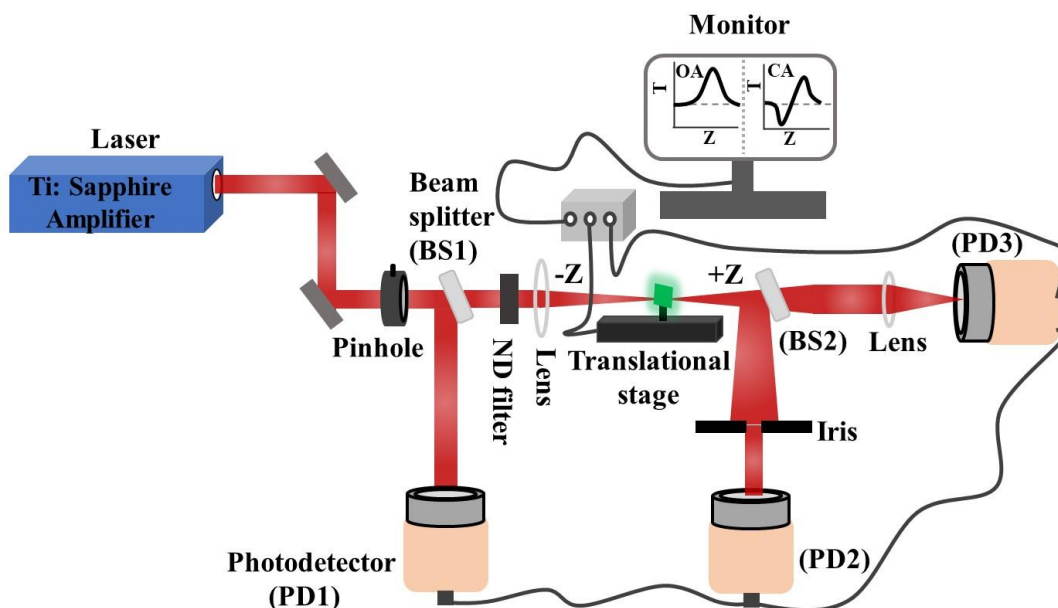


Figure 1. Cartoon depicting schematic of Z-scan setup.

PD1 (reference detector) and second one passes through the sample and again gets divided into two beams at beam splitter BS2. Finally, one beam goes into photodetector PD2 (close aperture configuration) and the second beam into photodetector PD3 (open aperture configuration). The laser beam was focused over the sample using a convex lens with a focal length of 10 cm. The beam waist was measured using a sensor and found to be 37- 40 μm at the focus. A computer controlled translational stage was used for scanning the samples. In each scan, sample was moved to the +ve and -ve sides of $Z = 0$ position. The optical powers were measured using a power meter (Model No. 1917-R) from Newport, USA. Z-scan curves were fitted using the MATLAB programme.

RESULTS AND DISCUSSION

Double perovskite $\text{Cs}_2\text{AgIn}_{0.9}\text{Bi}_{0.1}\text{Cl}_6$ NCs were synthesized according to a room-temperature antisolvent precipitation method (see supporting information) and characterized structurally and optically. Figure 2 (a) and (b) show low and high resolution TEM images of NCs along with their size distribution (inset of Figure 2 (a)). The average particle size was found to be 3.5

nm. The crystal lattice of NCs can be clearly viewed from the high-resolution scanning transmission electron microscopy (HRSTEM) image (Figure 2(b, c)). The fast Fourier transform (FFT) in Figure 2 (d) reveals a fcc structure of double perovskite NCs and shows that the NC depicted in Figure 2(b) is oriented in the [111] zone axis (ZA). The crystal structure of the double perovskites agrees well with the known structure for $\text{Cs}_2\text{AgInCl}_6$ in literature.³⁹ XRD and XPS measurements (Figure S1 (a) and (b), supporting information) further confirm the formation of NCs as described in previous reports.⁴⁰ The EDX elemental maps (Figure S1 (c), Table S1, supporting information) for Cs, Ag, In, Bi, and Cl, which were taken from the double perovskite NCs, additionally confirm the composition of the NCs.

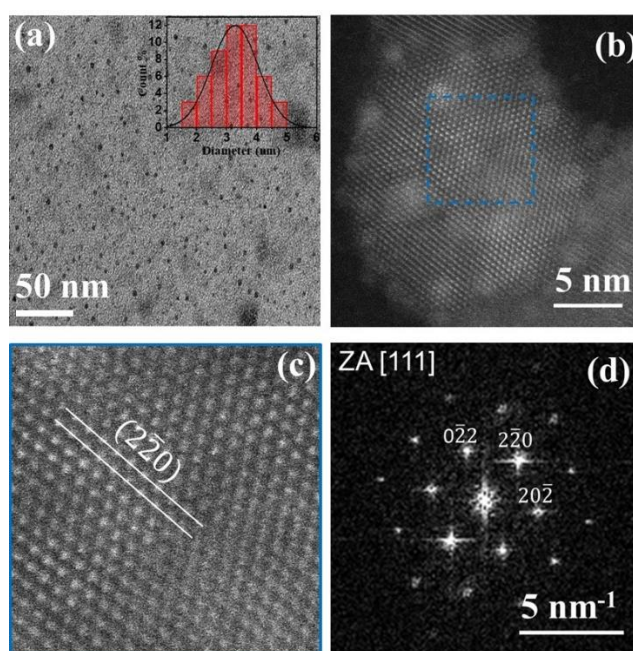


Figure 2. (a) TEM images of double perovskite NCs (inset represents histogram of particle size distribution). (b) HRSTEM image of a double perovskite NC. (c) Close-up of the area marked with a blue square in panel (b). The direction of the (2-20) planes are indicated by white lines. (d) FFT of the NC in panel (b) showing the [111] ZA.

Figure 3 (a) depicts the absorption spectrum of NCs in solution having a peak around 370 nm. The bandgap of the NCs was estimated from the Tauc plot (Inset of Figure 3(a)) and

found to be 3.0 eV. We recorded the corrected (see supporting information for details on the correction method) photoluminescence (PL) spectrum of the NC film exhibiting a broad orange coloured emission with a maximum at 630 nm as shown in Figure 3(b). Note that the uncorrected PL spectrum of the NCs (Figure S3(a), supporting information) is very similar to the existing report.⁴⁰ The origin of such emission has been reported to be the relaxation of charge carriers from allowed direct band states to forbidden states.⁴⁰ Further, a transient PL measurement was performed using time-correlated

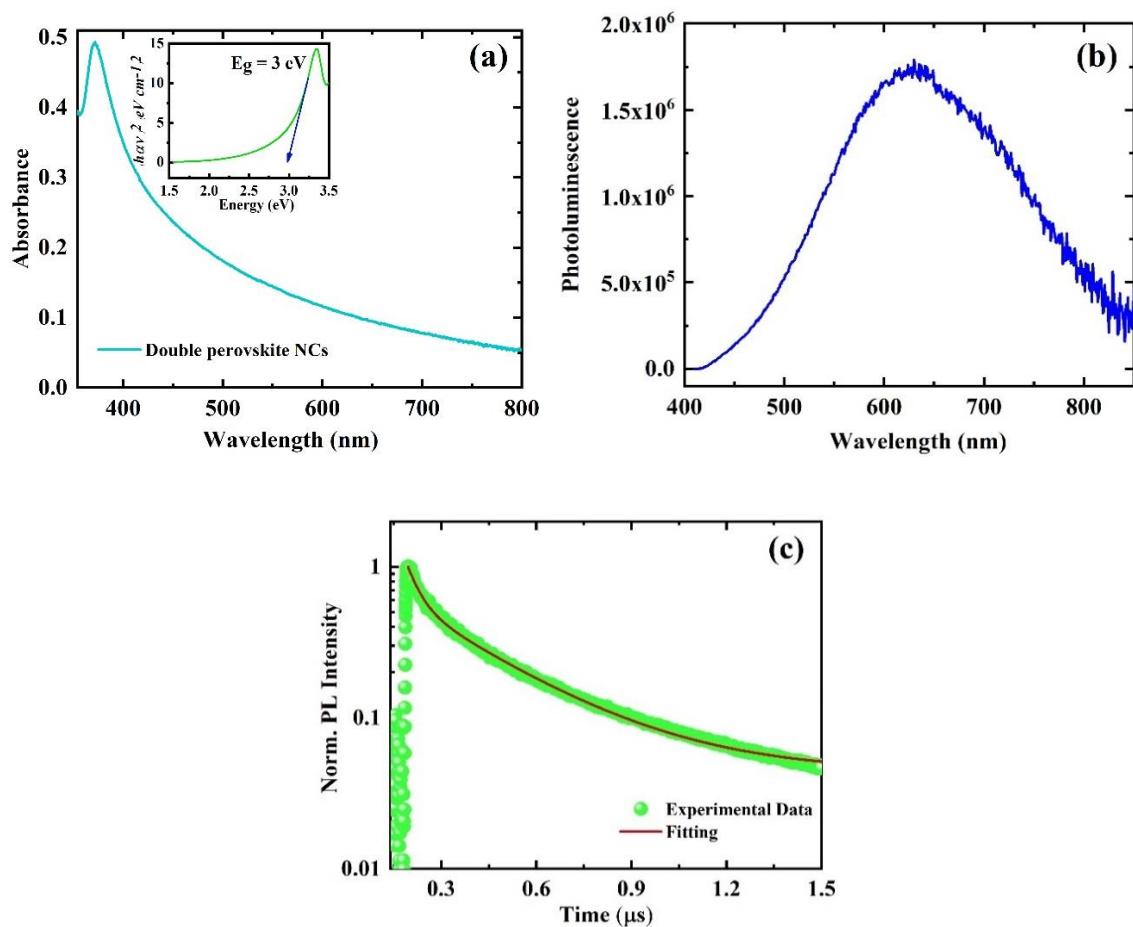


Figure 3. Absorption (a), and corrected photoluminescence (b) spectra of the double perovskite NCs. (c) PL decay trace of NCs recorded using TCSPC. Inset of figure 3(a) represents the Tauc plot.

single-photon counting (TCSPC) by exciting the sample with 355 nm laser pulses in the microsecond time window (Figure 3(c)). We fitted the curve using a biexponential function and found two time components; 40 ns (98.4 %) and 308 ns (1.6 %). The long lifetime component could be ascribed to parity forbidden transitions from the conduction band minimum to the valence band maximum.⁴¹

Next, we drop casted pre-synthesised NCs on a glass cover slip followed by drying. The average thickness of the NC film was measured to be 512 nm using scanning electron microscopy (SEM) (Figure S2, supporting information). Symmetric transmission curves shown in Figure 4 and S4 (supporting information) are OA Z-scan traces for NCs measured at 800 nm. As the input intensity increases, the transmission through the sample decreases and finally saturates at higher input intensities (Figure 4). Clearly, the data obtained at different input intensities indicate a reverse saturable absorption (RSA) behaviour of perovskite NCs. We kept the incident light intensities during the experiments to an optimal level to avoid supercontinuum generation and repeated the scan multiple times. Since the energy of the excitation light (1.55 eV) is below the bandgap (3.0 eV) of the NCs, the direct transition of electrons to the conduction band via one-photon absorption is not feasible. In fact, the absorption spectrum of the perovskite NCs film (Figure S3 (b), supporting information) shows that the one-photon absorption at 800 nm is negligible. The only means left for electrons to reach the conduction band is via two-photon absorption. Therefore, the observed optical nonlinearity at nonresonant excitation (at 800 nm) could be ascribed to the generation of bound or free carriers via two-photon absorption processes.

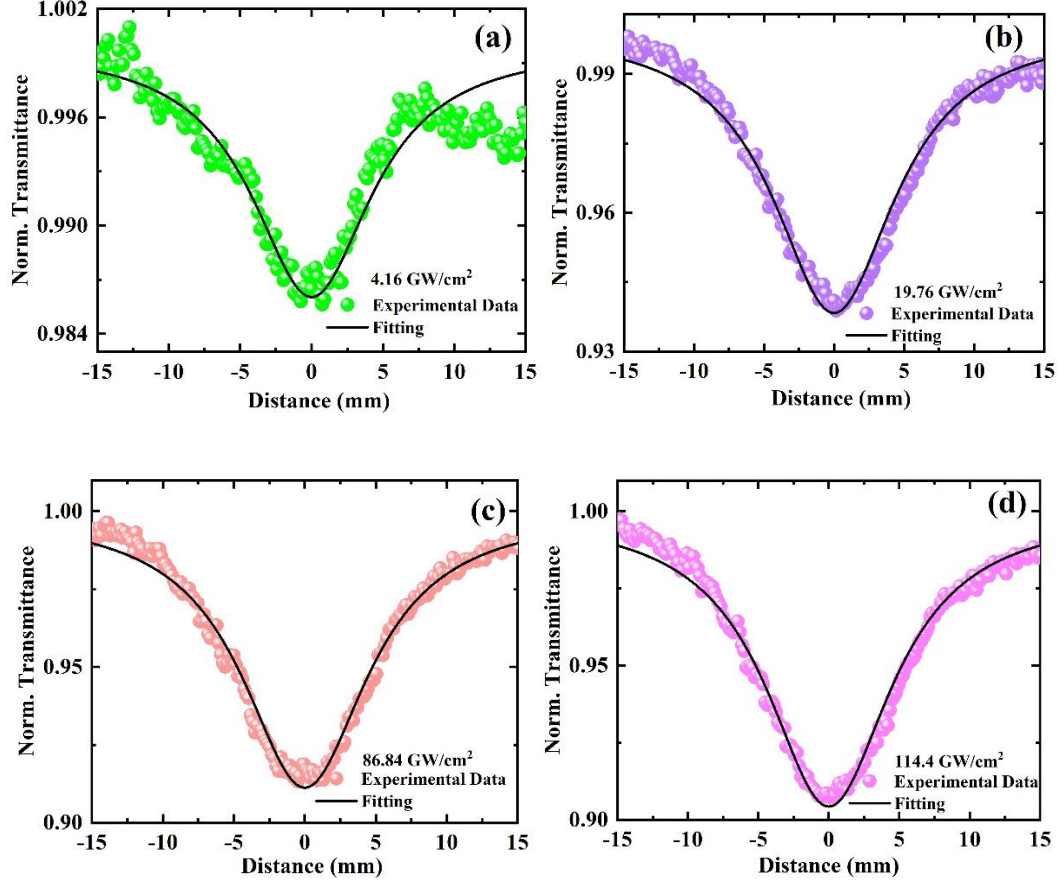


Figure 4. Open aperture (OA) Z-scan curves obtained at different input intensities: (a) 4.16, (b) 19.76, (c) 86.84 and (d) 114.4 GW/cm² at 800 nm following fs excitation.

To extract the TPA absorption coefficient, we have made use of the multi-photon absorption model,⁴²

$$T_{OA(nPA)} = \frac{1}{\left[1 + (n-1)\alpha_n L_{eff} \left(\frac{I_0}{1 + \left(\frac{z}{z_0}\right)^2} \right)^{n-1} \right]^{\frac{1}{n-1}}} \quad 1$$

where $L_{eff} = \frac{1 - e^{-\alpha_0 L}}{\alpha_0}$ is the effective path length of the sample, α_0 is the linear absorption

coefficient of the sample, $z_0 = \frac{\pi W_0^2}{\lambda}$ is the Rayleigh range which is calculated to be 4.8 mm,

w_0 is the beam width at the focus and calculated to be $33.05 \mu\text{m}$, and I_0 is the input peak intensity at the focus. The calculated value of effective path length (512 nm) is found to be much less than Rayleigh range (z_0) satisfying the thin film approximation $L_{\text{eff}} \ll z_0$.

OA data are fitted well using equation 1 with $n = 2$. The calculated values of the TPA coefficient (i.e., α_2 which is also assigned to β) are of the order of 10^{-9} cm/GW and are given in Table 1. It is noteworthy to mention that no nonlinearity has been observed from the glass cover slip at the highest input intensities used (Figure S4 (c), supporting information).

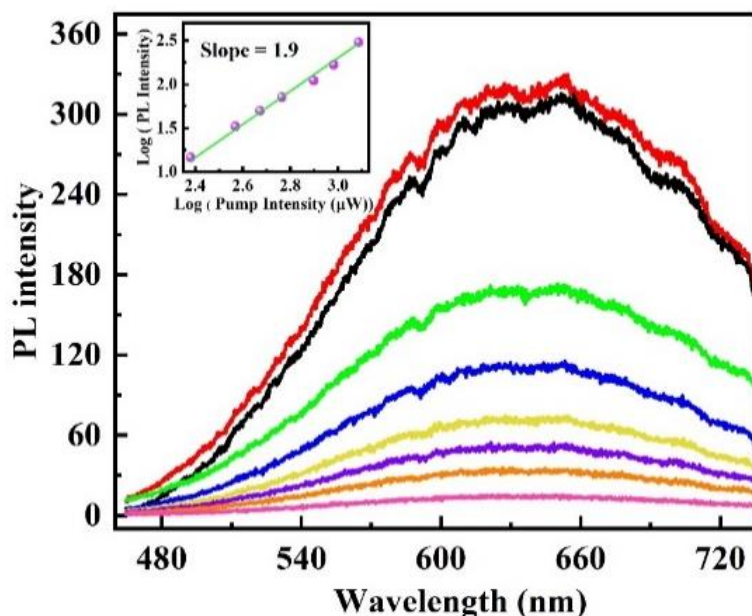


Figure 5. Fluorescence spectra of NCs film at different excitation intensities at 800 nm: 1510 μW (red curve), 1220 μW (black curve), 960 μW (green curve), 790 μW (blue curve), 580 μW (yellow curve), 470 μW (purple curve), 370 μW (orange curve) and 240 μW (pink curve). The inset represents the logarithmic plot of excitation-power dependent PL.

Further, to validate the TPA response of our sample, we measured fluorescence following 800 nm laser excitation (Figure 5). The NC film exhibits a broad emission band with a maximum around 630 nm. It is worth mentioning that the observed two-photon PL is consistent with the one observed following high energy (3.2 eV) single-photon excitation as

shown in Figure 3 (b). Since the linear absorption at 800 nm is negligible, the observed fluorescence is attributed to TPA. To further confirm the TPA process, the power dependent fluorescence intensity of our sample was measured. The logarithmic plot of the fluorescence intensity versus input power with a slope of 1.9 (Inset of Figure 5) further indicates that the mechanism responsible for the observed emission at 800 nm excitation is TPA.

We calculated the TPA cross-section (σ_{TPA}) using the following equation⁴²

$$\sigma_{TPA} = \frac{(h\omega)}{N} \beta \quad 2$$

Here, ω is the frequency of laser radiation and N is the concentration of NCs. Obtained values of the TPA cross-section are in the range of 10^4 GM (Table1).

To account for the optical limiting effect, transmission curves are drawn as a function of the input fluence at each excitation intensity (Figure S5, supporting information). The light fluence $F(z)$ at any position z of the incident beam with energy E_{in} was calculated from the expression⁴³

$$F(z) = \frac{4\sqrt{\log 2} E_{in}}{\pi^{3/2} w(z)^2} \quad 3$$

Where the beam radius $w(z)$ is given by

$$w(z) = w(0) \left[1 + \left(z / z_0 \right)^2 \right]^{1/2} \quad 4$$

The decrease in the transmission with the increase in input fluence (Figure S5, supporting information) demonstrates the optical limiting behaviour of perovskite NCs. The optical limit offset at which transmission starts to decrease substantially represents the optical limiting

quality of a material. The values of the optical limiting offset of the double perovskite NCs are presented in Table 1.

Next, Figure 6 represents the closed-aperture (CA) measurements performed on the NCs. The CA curves exhibit a valley-peak type structure. The observed prefocal transmission minimum (valley) followed by a transmission maximum (peak) bears the Z-scan signature of positive refractive nonlinearity (with the nonlinear refractive index, $n_2 > 0$).

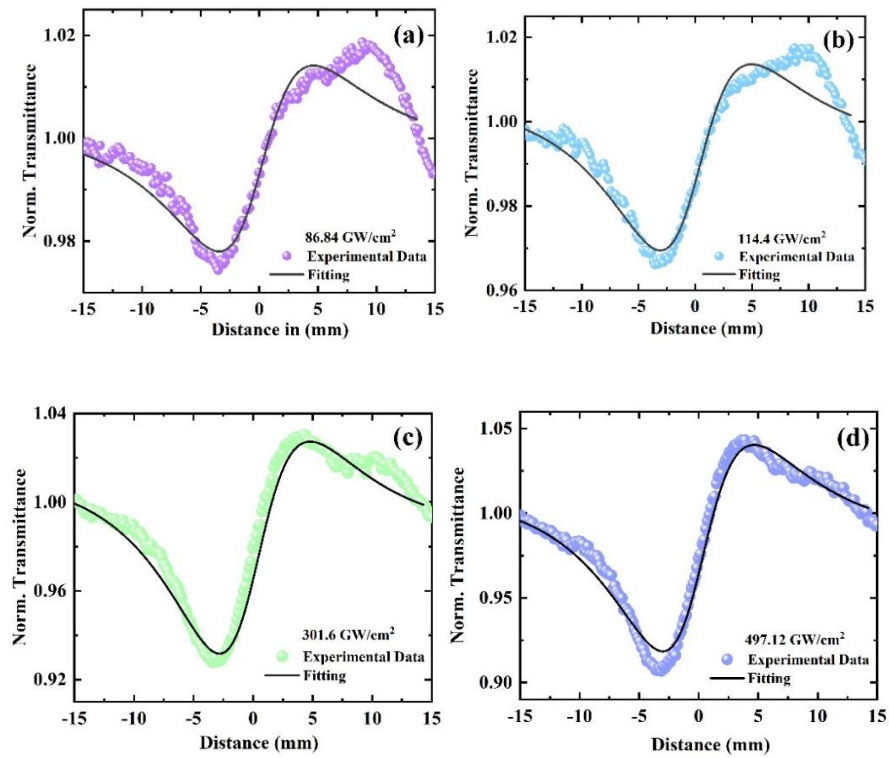


Figure 6. Closed-aperture (CA) Z-scan curves obtained with fs laser excitation at 800 nm having different intensities.

To extract the values of n_2 , CA traces were fitted using the following analytically derived equation⁴⁴

$$T_{CA} = 1 + \frac{4x\Delta\phi_0}{(x^2+9)(x^2+1)} - \frac{2(x^2+3)\Delta\psi_0}{(x^2+9)(x^2+1)} \quad 5$$

Here, $\Delta\phi_0 = kn_2I_0L_{eff}$ is the on-axis phase shift at the focus, $k = \frac{2\pi}{\lambda}$, $\Delta\psi_0 = \frac{\beta I_0 L_{eff}}{2}$ is the phase change due to nonlinear absorption, β is the two-photon absorption coefficient and $x = \frac{z}{z_0}$. Good fitting of the CA curves with equation 5 infers that the asymmetric transmission behaviour in NCs could be due to strong TPA.⁴⁵ The estimated value of n_2 is in the range of $0.55\text{-}2.6 \times 10^{-13} \text{ cm}^2/\text{W}$ (Table 1). We must note that the fitting of the CA data is not as good as the OA Z-scan. The fitting error could be attributed to the presence of a second peak in the CA Z-scan curve at $\sim 9 \text{ mm}$ (Figure 6 (a) and (b)). Actually, the non-uniformity in the film thickness causes the distortion of Gaussian profile of the laser beam and thereby induces such artefact in the CA profile.⁴⁶ Overall errors in these measurements and hence in the values of NLO coefficients are estimated to be $\pm 10\text{-}15\%$ and may arise mainly from input laser fluctuation, estimating peak intensities and fitting errors.

Table 1. Summary of NLO coefficients (TPA cross-section along with real and imaginary parts of susceptibility and optical limiting onsets) of NCs

S.No.	$I_0 \left(\frac{GW}{cm^2} \right)$	$\beta \times 10^{-9} \left(\frac{cm}{W} \right)$	$n_2 \times 10^{-13} \left(\frac{cm^2}{W} \right)$	$\sigma_{TPA} \times 10^4 \text{ (GM)}$	$\text{Re } \chi^{(3)} \times 10^{-11} \left(\frac{m^2}{W} \right)$	$\text{Im } \chi^{(3)} \times 10^{-11} \left(\frac{m}{W} \right)$	Limiting offset $\left(\frac{mJ}{cm^2} \right)$
1	4.16	66.43	-	3.11	-	14	0.06
2	19.76	64.93	-	3.0	-	13.6	0.15
3	86.84	21.90	2.6	1.02	1.37	4.60	0.7
4	114.4	18.061	2.4	0.84	1.26	3.79	1.5
5	301.6	6.88	0.55	0.32	0.29	1.44	2.6

The real and imaginary parts of the third-order nonlinear susceptibility were calculated using the following relations⁴⁷

$$\text{Re } \chi^{(3)}(esu) = \frac{cn_0^2}{120\pi^2} n_2 \left(\frac{m^2}{W} \right) \quad 6$$

$$\text{Im } \chi^{(3)}(esu) = \frac{c^2 n_0^2}{240\pi^2 \omega} \beta \left(\frac{m}{W} \right) \quad 7$$

Here, n_0 is the linear refractive index and c is the speed of the light. Since the exact value of n_0 for $\text{Cs}_2\text{AgIn}_{0.9}\text{Bi}_{0.1}\text{Cl}_6$ NCs is unknown, we have used the value $n_0 = 1.44$ of the same class of material as reference.⁴⁸ The calculated values of n_2 are listed in Table 1.

To exact the superior nonlinear optical behaviour of the double perovskite NCs, a comparison of the NLO parameters is made with the reported materials (Table 2). Clearly, the TPA coefficient of $\text{Cs}_2\text{AgIn}_{0.9}\text{Bi}_{0.1}\text{Cl}_6$ NCs is ~2-3 orders of magnitude larger than InP/ZnS quantum dots (QDs) and 5 orders of magnitude larger than ZnSe QDs. The TPA cross-section is found to be a few orders of magnitude higher than InP/ZnS QDs and CdTe QDs.⁴⁹ Similarly, the TPA coefficient of our perovskite NCs is much larger than CsPbBr_3 NCs and nanorods, and $\text{CsPb}(\text{Cl}_{0.53}\text{Br}_{0.47})_3$ NCs.⁵⁰ It is apparent from Table 2 that the value of the TPA coefficient of our NCs is higher than alternative materials. The lower value of the TPA cross-section of the double perovskite NCs could be the consequence of a reduced density of states due to large quantum confinement in small sized particles.⁵¹

Figure 7 (a) depicts the variation of the TPA coefficient as a function of the input intensity. It is inferred from the figure that with an increase in input fluence, β decreases and

tends to saturate at higher intensities. Nonetheless, n_2 decreases with the increment of intensity (Table 1) due to its direct dependence on the charge carrier density. In fact, the effective nonlinear refractive index is given by the following relation⁵²

$$n_2^* = n_2 + \frac{\xi_\gamma N(t)}{I} \quad 8$$

Here, n_2^* is the effective nonlinear refractive index, $N(t)$ is the photoexcited carrier density, ξ_γ is the change in refractive index per unit density of conduction band electrons and I is the input intensity. Free carriers can alter the refractive index because of their capability to absorb light.⁵³ In nonresonant excitation, the dominant pathway for the generation of free carriers is multiphoton absorption, whereas in resonant conditions, the generation takes place via linear absorption.

Table 2. Comparison of NLO properties of double perovskite NCs with other nanomaterials

Material	Excitation	$\beta \left(\frac{cm}{W} \right)$	$n_2 \left(\frac{cm^2}{W} \right)$	$\sigma_{TPA} (GM)$	Ref
Cs ₂ AgIn _{0.9} Bi _{0.1} Cl ₆	800 nm, 1 kHz, 58 fs	21.90×10 ⁻⁹	2.6×10 ⁻¹³	1.02×10 ⁴	Present work
CsPbBr ₃ NCs	800 nm, 1 kHz, 70 fs	180×10 ⁻¹¹	10 ⁻⁹	98×10 ⁴	54

CsPbBr ₃ nanorods	800 nm, 1 kHz, 70fs	0.71×10 ⁻¹¹	---	0.2×10 ⁴	54
CsPbBr ₃ 0.03% and 0.05% Ni doped	800 nm, 1 kHz, 70 fs	3.8×10 ⁻¹¹	7.9×10 ⁻¹²	1.56×10 ⁴	32
		3.9×10 ⁻¹¹	8.4×10 ⁻¹¹	1.6×10 ⁴	

CsPbCl ₂ Br	800 nm, 1 kHz, 50 fs	5.4×10^{-11}	---	1.1×10^5	55
CsPbClBr ₂		6.4×10^{-11}	---	1.6×10^5	
CsPbBr ₃ QDs		9.1×10^{-11}	---	2.2×10^5	
Fe ³⁺ doped	800 nm, 1 kHz, 140 fs	210×10^{-9}	---	---	56
CsPb(Cl/Br) ₃ microwires					
CsPbBr ₃ R-Perov-NC	800 nm, 1 kHz, 100 fs	---	---	3.68×10^4	57
CH ₃ NH ₄ PbBr ₃	800 nm, 1 kHz, 140 fs	8.6×10^{-9}	---	---	58
Single crystal					
CdSeTe QDs	800 nm, 1 kHz, 120 fs				59
4 nm		4.2×10^{-10}	---	---	
5 nm in size		3.55×10^{-9}	---	---	
ZnSe QDs	800 nm, 10 Hz, 100 fs	7.9×10^{-14}	---	0.49×10^4	60
4.5 nm in size					
ZnSe/ZnS	800 nm, 10 Hz, 100 fs	8.2×10^{-14}	---		60
Core/shell				0.51×10^4	
4.5 nm in size					
CuS QDs	800 nm, 10 kHz, 100 fs	2.3×10^{-12}	---	---	61
InP/ZnS QDs	800 nm, 1 kHz, 100 fs				51
2.2 nm		9.0×10^{-12}	-0.57×10^{-15}	3.5×10^3	
2.8 nm in size		1.2×10^{-11}	-0.71×10^{-15}	6.2×10^3	

In case of nonresonant (fs) excitation, the low intensity regime contribution to the nonlinearity is assigned to bound charge carriers, while at a high intensity regime, the nonlinearity from free carriers dominates because free charge carriers accumulate during the pulse.⁶² On contrary, for nanosecond pulses, free carriers disguise the contribution from bound electronic charges and become primary contributors to optical nonlinearity. In the low intensity regime, the TPA is weak and $N(t)$ is almost constant, therefore, an increase in excitation power causes n_2^* to decrease in accordance with equation 8. However, in the high intensity regime, the growth of $N(t)$ is slowly counterbalanced with the increase of the excitation intensity and n_2^* decreases again with the increase of excitation intensity. It is worth noting that we have taken into account the contribution of the nonlinear refraction from the cover slip by subtracting its value from the sample. At the highest intensity (497.12 GW / cm^2), the negative value of n_2 is due to decreased transmission ($\Delta T_{p-v} = T_{peak} - T_{valley}$) of NCs as compared to the cover slip (Figure S6, supporting information).^{50, 51}

To examine the observed saturation of TPA in more detail, we utilized an alternative technique. We measured the transmitted intensity at each incident peak intensity by directly placing the sample at the beam waist of a focused laser beam. Figure 7(b) represents the plot of the inverse transmission vs intensity for the NCs. A typical TPA feature, i.e., inverse transmission, increases as the input intensity gradually increases, is observed. Light attenuation for degenerate TPA in a material is described by⁵⁸

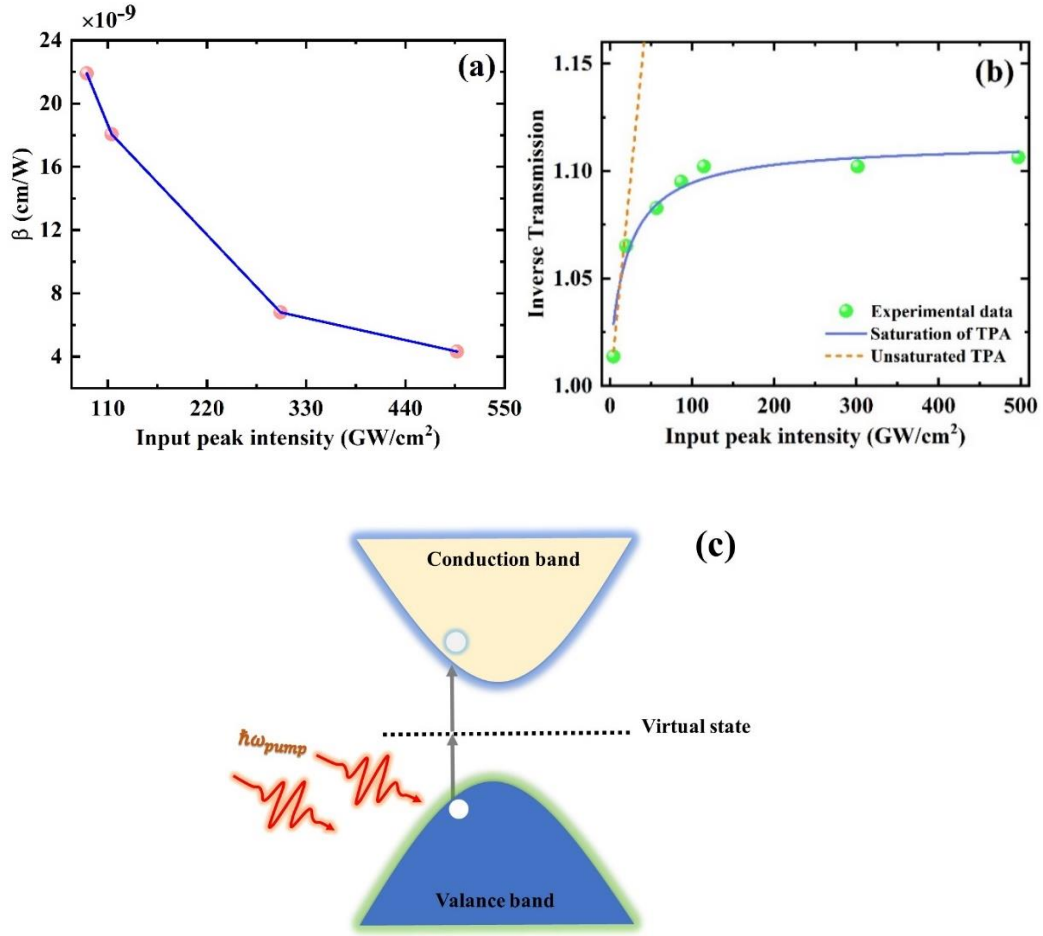


Figure 7. (a) Variation of TPA coefficient (β) as a function of the peak intensity of the input light. (b) Plot of inverse transmission vs input peak intensity fitted with saturation (solid blue line) and non-saturation TPA (dotted orange line) models. (c) Schematic of the TPA process in double perovskite NCs under light (800 nm) illumination.

$$\frac{dI(z)}{dz} = -\alpha_0 I(z) - \beta I^2(z) \quad 9$$

Where $I(z)$ is the peak intensity, α_0 is the linear absorption coefficient and β is the TPA coefficient. The solution of the above differential equation can be expressed as ⁵⁸

$$T(I) = \frac{e^{-\alpha_0 L}}{\beta I L_{\text{eff}} + 1} \quad 10$$

Here, L is the path length and L_{eff} is the effective path length. The equation above can more accurately be expressed by taking into account possible reflection and scattering which lead to the reduction of light intensity entering the sample by the factor $(1-R)$, where R is the reduction factor caused by scattering and reflection, as ⁶³

$$T(I) = \frac{(1-R)^2 e^{-\alpha_0 L}}{(1-R)\beta I L_{eff} + 1} \quad 11$$

In the low-intensity regime, inverse transmission increases linearly (Figure 7(b)) in accordance with equation 11 conforming the presence of TPA. On increasing the intensity further, the transmission through the sample becomes stabilized giving a signature of TPA saturation. In this scenario, the TPA coefficient can be expressed as ⁶⁴

$$\beta(I) = \frac{\beta_0}{1 + \frac{I}{I_{sat}}} \quad 12$$

Here, β_0 is the nonsaturation TPA coefficient and I_{sat} is the saturation intensity. The nonsaturation TPA model (equation 11) alone was unable to fit the experimental data (dotted line in Figure 7(b)). Therefore, we combined both the TPA saturation model (equation 12) and equation 11 to support our data. Equations 11 and 12 together fit well the experimental data as shown in Figure 7(b). The value of β_0 obtained from fitting is 74.32 cm/GW and the corresponding TPA saturation intensity is 23.11 GW/cm^2 . The mechanism of the TPA process is schematically shown in Figure 7(c).

CONCLUSIONS

In this work, we have investigated third-order nonlinear optical properties of $\text{Cs}_2\text{AgIn}_{0.9}\text{Bi}_{0.1}\text{Cl}_6$ double perovskite NCs in the femtosecond regime by employing a Z-scan technique. Under nonresonant excitation, observed nonlinearities are attributed to bound charges generated in

the low-intensity regime. However, at higher intensities, nonlinearity is due to free carriers and the TPA process. The nonlinear refractive index of perovskite NCs decreases with the increase of excitation intensity due to the variation in charge carrier density. Furthermore, we observe the saturation of TPA in the perovskite NCs. The large values of the TPA coefficient and cross-section demonstrate the prospect of this material for applications involving multiphoton bioimaging and upconverted lasing.

Supporting Information

Synthesis of NCs, experimental details, SEM image of NC film, optical limiting curves of perovskite NCs, OA and CA Z-scan data of cover slip.

Corresponding Authors

Suman Kalyan Pal- School of Basic Sciences and Advanced Material Research Center, Indian Institute of Technology Mandi, Kamand 175005, H.P, India.

Email: suman@iitmandi.ac.in

Authors

Aamir Mushtaq- School of Basic Sciences and Advanced Material Research Center, Indian Institute of Technology Mandi, Kamand 175005, H.P, India.

Bapi Pradhan- Department of Chemistry, KU Leuven, Celestijnenlaan 200F, 3001 Heverlee, Belgium.

Dushyant Kushavah- School of Basic Sciences and Advanced Material Research Center, Indian Institute of Technology Mandi, Kamand 175005, H.P, India.

Yiyue Zhang- Department of Chemistry, KU Leuven, Celestijnenlaan 200F, 3001 Heverlee, Belgium.

Mathias Wolf- Department of Chemistry, KU Leuven, Celestijnenlaan 200F, 3001 Heverlee, Belgium

Nadine Schrenker- Electron Microscopy for Materials Research, University of Antwerp, Groenenborgerlaan, 171, 2020 Antwerp, Belgium

Eduard Fron- Department of Chemistry, KU Leuven, Celestijnenlaan 200F, 3001 Heverlee, Belgium

Sara Bals- Electron Microscopy for Materials Research, University of Antwerp, Groenenborgerlaan, 171, 2020 Antwerp, Belgium

Johan Hofkens- Department of Chemistry, KU Leuven, Celestijnenlaan 200F, 3001 Heverlee, Belgium.

Elke Debroye- Department of Chemistry, KU Leuven, Celestijnenlaan 200F, 3001 Heverlee, Belgium

Max Planck Institute for Polymer Research, Ackermannweg 10, 55128 Mainz, Germany.

Author Contributions

These authors contributed equally

Acknowledgments

A.M. is thankful to IIT Mandi for his fellowship and Advanced Materials Research Centre for the experimental facilities. A.M is also thankful to Torbjörn Pascher (Pascher Instrument) for writing Z-scan data acquisition program. J.H. acknowledges financial support from the Research Foundation-Flanders (FWO, Grant No. G983.19N, G0A5817N, and G0H6316N) and the Flemish government through long-term structural funding Methusalem (CASAS2, Meth/15/04). B.P. acknowledges postdoctoral fellowship from the Research Foundation-

Flanders (FWO Grant No. 1275521N). D.K. acknowledges the financial support from Science and Engineering Research Board (Grant No. PDF/2018/003146), India.

References

1. Liang, G.; Hu, X.; Yu, X.; Shen, Y.; Li, L. H.; Davies, A. G.; Linfield, E. H.; Liang, H. K.; Zhang, Y.; Yu, S. F.; Wang, Q. J., Integrated Terahertz Graphene Modulator with 100% Modulation Depth. *ACS Photonics* **2015**, *2* (11), 1559-1566.
2. Mascheck, M.; Schmidt, S.; Silies, M.; Yatsui, T.; Kitamura, K.; Ohtsu, M.; Leipold, D.; Runge, E.; Lienau, C., Observing the localization of light in space and time by ultrafast second-harmonic microscopy. *Nat. Photon.* **2012**, *6* (5), 293-298.
3. Song, Y.; Chen, Y.; Jiang, X.; Ge, Y.; Wang, Y.; You, K.; Wang, K.; Zheng, J.; Ji, J.; Zhang, Y.; Li, J.; Zhang, H., Nonlinear Few-Layer MXene-Assisted All-Optical Wavelength Conversion at Telecommunication Band. *Adv. Opt. Mater.* **2019**, *7* (18), 1801777.
4. Nayak, A.; Park, J.; De Mey, K.; Hu, X.; Duncan, T. V.; Beratan, D. N.; Clays, K.; Therien, M. J., Large Hyperpolarizabilities at Telecommunication-Relevant Wavelengths in Donor–Acceptor–Donor Nonlinear Optical Chromophores. *ACS Cent. Sci.* **2016**, *2* (12), 954-966.
5. Ye, W.; Zeuner, F.; Li, X.; Reineke, B.; He, S.; Qiu, C.-W.; Liu, J.; Wang, Y.; Zhang, S.; Zentgraf, T., Spin and wavelength multiplexed nonlinear metasurface holography. *Nat. Commun.* **2016**, *7* (1), 11930.
6. Xu, J.; Li, X.; Xiong, J.; Yuan, C.; Semin, S.; Rasing, T.; Bu, X. H., Halide Perovskites for Nonlinear Optics. *Adv. Mater.* **2020**, *32* (3), 1806736.
7. Shi, J.; Yu, P.; Liu, F.; He, P.; Wang, R.; Qin, L.; Zhou, J.; Li, X.; Zhou, J.; Sui, X.; Zhang, S.; Zhang, Y.; Zhang, Q.; Sum, T. C.; Qiu, X.; Liu, Z.; Liu, X., 3R MoS₂ with Broken Inversion Symmetry: A Promising Ultrathin Nonlinear Optical Device. *Adv. Mater.* **2017**, *29* (30), 1701486.

8. Quan, C.; Lu, C.; He, C.; Xu, X.; Huang, Y.; Zhao, Q.; Xu, X., Band Alignment of MoTe₂/MoS₂ Nanocomposite Films for Enhanced Nonlinear Optical Performance. *Adv. Mater. Interfaces* **2019**, *6* (5), 1801733.
9. Zhao, M.; Peng, R.; Zheng, Q.; Wang, Q.; Chang, M.-J.; Liu, Y.; Song, Y.-L.; Zhang, H.-L., Broadband optical limiting response of a graphene–PbS nanohybrid. *Nanoscale* **2015**, *7* (20), 9268-9274.
10. Zheng, C.; Lei, L.; Huang, J.; Chen, W.; Li, W.; Wang, H.; Huang, L.; Huang, D., Facile control of metal nanoparticles from isolated nanoparticles to aggregated clusters on two-dimensional graphene to form optical limiters. *J. Mater. Chem. C* **2017**, *5* (44), 11579-11589.
11. Zhao, G.; Zhang, F.; Wu, Y.; Hao, X.; Wang, Z.; Xu, X., One-Step Exfoliation and Hydroxylation of Boron Nitride Nanosheets with Enhanced Optical Limiting Performance. *Adv. Opt. Mater.* **2016**, *4* (1), 141-146.
12. Shi, J.-m.; Xu, W.; Liu, Q.-y.; Liu, F.-l.; Huang, Z.-l.; Lei, H.; Yu, W.-t.; Fang, Q., Polynitrile-bridged two-dimensional crystal: Eu(III) complex with strong fluorescence emission and NLO property. *Chem. Commun.* **2002**, (7), 756-757.
13. Wang, C.; Zhang, T.; Lin, W., Rational Synthesis of Noncentrosymmetric Metal–Organic Frameworks for Second-Order Nonlinear Optics. *Chem. Rev.* **2012**, *112* (2), 1084-1104.
14. Ravindran, S.; Datta, A.; Alameh, K.; Lee, Y. T., GaAs based long-wavelength microring resonator optical switches utilising bias assisted carrier-injection induced refractive index change. *Opt. Express* **2012**, *20* (14), 15610-15627.
15. Geldenhuys, R.; van der Merwe, J. S.; Thakulsukanant, K.; Wang, Z.; Chi, N.; Yu, S., Contention resolution and variable length optical packet switching using the active vertical-coupler-based optical Crosspoint switch. *Opt. Switch. Netw* **2011**, *8* (2), 86-92.

16. Shin, S.; Su, C., Strong increase of the derivative of the carrier-induced index change of semiconductor lasers at low injected carrier density. *IEEE Photonics Technol. Lett.* **1993**, *5* (9), 981-983.
17. Miller, A.; Welford, K.; Daino, B., *Nonlinear optical materials and devices for applications in information technology*. Springer Science & Business Media: 2013; Vol. 289.
18. Zhou, Y.; Huang, Y.; Xu, X.; Fan, Z.; Khurgin, J. B.; Xiong, Q., Nonlinear optical properties of halide perovskites and their applications. *Appl. Phys. Rev.* **2020**, *7* (4), 041313.
19. Walters, G.; Sargent, E. H., Electro-optic Response in Germanium Halide Perovskites. *J. Phys. Chem. Lett.* **2018**, *9* (5), 1018-1027.
20. Manser, J. S.; Christians, J. A.; Kamat, P. V., Intriguing Optoelectronic Properties of Metal Halide Perovskites. *Chem. Rev.* **2016**, *116* (21), 12956-13008.
21. Stranks, S. D.; Hoye, R. L. Z.; Di, D.; Friend, R. H.; Deschler, F., The Physics of Light Emission in Halide Perovskite Devices. *Adv. Mater.* **2019**, *31* (47), 1803336.
22. Galkowski, K.; Mitioglu, A.; Miyata, A.; Plochocka, P.; Portugall, O.; Eperon, G. E.; Wang, J. T.-W.; Stergiopoulos, T.; Stranks, S. D.; Snaith, H. J.; Nicholas, R. J., Determination of the exciton binding energy and effective masses for methylammonium and formamidinium lead tri-halide perovskite semiconductors. *Energy Environ. Sci.* **2016**, *9* (3), 962-970.
23. Qi, X.; Zhang, Y.; Ou, Q.; Ha, S. T.; Qiu, C.-W.; Zhang, H.; Cheng, Y.-B.; Xiong, Q.; Bao, Q., Photonics and Optoelectronics of 2D Metal-Halide Perovskites. *Small* **2018**, *14* (31), 1800682.
24. Jiang, G.; Miao, L.; Yi, J.; Huang, B.; Peng, W.; Zou, Y.; Huang, H.; Hu, W.; Zhao, C.; Wen, S., Ultrafast pulse generation from erbium-doped fiber laser modulated by hybrid organic–inorganic halide perovskites. *Appl. Phys. Lett.* **2017**, *110* (16), 161111.

25. Li, P.; Chen, Y.; Yang, T.; Wang, Z.; Lin, H.; Xu, Y.; Li, L.; Mu, H.; Shivananju, B. N.; Zhang, Y.; Zhang, Q.; Pan, A.; Li, S.; Tang, D.; Jia, B.; Zhang, H.; Bao, Q., Two-Dimensional $\text{CH}_3\text{NH}_3\text{PbI}_3$ Perovskite Nanosheets for Ultrafast Pulsed Fiber Lasers. *ACS Appl. Mater. Interfaces* **2017**, *9* (14), 12759-12765.
26. Dohner, E. R.; Jaffe, A.; Bradshaw, L. R.; Karunadasa, H. I., Intrinsic White-Light Emission from Layered Hybrid Perovskites. *J. Am. Chem. Soc.* **2014**, *136* (38), 13154-13157.
27. Li, X.; Wu, Y.; Zhang, S.; Cai, B.; Gu, Y.; Song, J.; Zeng, H., CsPbX_3 Quantum Dots for Lighting and Displays: Room-Temperature Synthesis, Photoluminescence Superiorities, Underlying Origins and White Light-Emitting Diodes. *Adv. Funct. Mater.* **2016**, *26* (15), 2435-2445.
28. Wang, Y.; Li, X.; Zhao, X.; Xiao, L.; Zeng, H.; Sun, H., Nonlinear Absorption and Low-Threshold Multiphoton Pumped Stimulated Emission from All-Inorganic Perovskite Nanocrystals. *Nano Lett.* **2016**, *16* (1), 448-453.
29. He, T.; Li, J.; Ren, C.; Xiao, S.; Li, Y.; Chen, R.; Lin, X., Strong two-photon absorption of Mn-doped CsPbCl_3 perovskite nanocrystals. *Appl. Phys. Lett.* **2017**, *111* (21), 211105.
30. Han, X.; Zheng, Y.; Chai, S.; Chen, S.; Xu, J., 2D organic-inorganic hybrid perovskite materials for nonlinear optics. *Nanophotonics* **2020**, *9* (7), 1787-1810.
31. Yi, J.; Miao, L.; Li, J.; Hu, W.; Zhao, C.; Wen, S., Third-order nonlinear optical response of $\text{CH}_3\text{NH}_3\text{PbI}_3$ perovskite in the mid-infrared regime. *Opt. Mater. Express* **2017**, *7* (11), 3894-3901.
32. Ketavath, R.; Katturi, N. K.; Ghugal, S. G.; Kolli, H. K.; Swetha, T.; Soma, V. R.; Murali, B., Deciphering the Ultrafast Nonlinear Optical Properties and Dynamics of Pristine and Ni-Doped CsPbBr_3 Colloidal Two-Dimensional Nanocrystals. *J. Phys. Chem. Lett.* **2019**, *10* (18), 5577-5584.

33. Noel, N. K.; Stranks, S. D.; Abate, A.; Wehrenfennig, C.; Guarnera, S.; Haghighirad, A.-A.; Sadhanala, A.; Eperon, G. E.; Pathak, S. K.; Johnston, M. B., Lead-free organic–inorganic tin halide perovskites for photovoltaic applications. *Energy Environ. Sci.* **2014**, *7* (9), 3061-3068.
34. Hao, F.; Stoumpos, C. C.; Cao, D. H.; Chang, R. P. H.; Kanatzidis, M. G., Lead-free solid-state organic–inorganic halide perovskite solar cells. *Nat. Photon.* **2014**, *8* (6), 489-494.
35. Jellicoe, T. C.; Richter, J. M.; Glass, H. F. J.; Tabachnyk, M.; Brady, R.; Dutton, S. E.; Rao, A.; Friend, R. H.; Credgington, D.; Greenham, N. C.; Böhm, M. L., Synthesis and Optical Properties of Lead-Free Cesium Tin Halide Perovskite Nanocrystals. *J. Am. Chem. Soc.* **2016**, *138* (9), 2941-2944.
36. Leng, M.; Chen, Z.; Yang, Y.; Li, Z.; Zeng, K.; Li, K.; Niu, G.; He, Y.; Zhou, Q.; Tang, J., Lead-Free, Blue Emitting Bismuth Halide Perovskite Quantum Dots. *J. Angew. Chem. Int. Ed.* **2016**, *55* (48), 15012-15016.
37. Zhang, J.; Yang, Y.; Deng, H.; Farooq, U.; Yang, X.; Khan, J.; Tang, J.; Song, H., High Quantum Yield Blue Emission from Lead-Free Inorganic Antimony Halide Perovskite Colloidal Quantum Dots. *ACS Nano* **2017**, *11* (9), 9294-9302.
38. Mushtaq, A.; Kushavah, D.; Ghosh, S.; Pal, S. K., Nonlinear optical properties of benzylamine lead(II) bromide perovskite microdisks in femtosecond regime. *Appl. Phys. Lett.* **2019**, *114* (5), 051902.
39. Gray, M. B.; Majher, J. D.; Strom, T. A.; Woodward, P. M., Broadband White Emission in $\text{Cs}_2\text{AgIn}_{1-x}\text{Bi}_x\text{Cl}_6$ Phosphors. *Inorg. Chem.* **2019**, *58* (19), 13403-13410.
40. Yang, B.; Mao, X.; Hong, F.; Meng, W.; Tang, Y.; Xia, X.; Yang, S.; Deng, W.; Han, K., Lead-Free Direct Band Gap Double-Perovskite Nanocrystals with Bright Dual-Color Emission. *J. Am. Chem. Soc.* **2018**, *140* (49), 17001-17006.

41. Luo, J.; Li, S.; Wu, H.; Zhou, Y.; Li, Y.; Liu, J.; Li, J.; Li, K.; Yi, F.; Niu, G.; Tang, J., Cs₂AgInCl₆ Double Perovskite Single Crystals: Parity Forbidden Transitions and Their Application For Sensitive and Fast UV Photodetectors. *ACS Photonics* **2018**, *5* (2), 398-405.
42. Krishnakanth, K. N.; Seth, S.; Samanta, A.; Venugopal Rao, S., Broadband ultrafast nonlinear optical studies revealing exciting multi-photon absorption coefficients in phase pure zero-dimensional Cs₄PbBr₆ perovskite films. *Nanoscale* **2019**, *11* (3), 945-954.
43. Philip, R.; Chantharasupawong, P.; Qian, H.; Jin, R.; Thomas, J., Evolution of Nonlinear Optical Properties: From Gold Atomic Clusters to Plasmonic Nanocrystals. *Nano Lett.* **2012**, *12* (9), 4661-4667.
44. Tripathy, U.; Bisht, P. B., Simultaneous estimation of optical nonlinear refractive and absorptive parameters by solvent induced changes in optical density. *Opt. Commun.* **2006**, *261* (2), 353-358.
45. Mukundam, V.; Sa, S.; Kumari, A.; Das, R.; Venkatasubbaiah, K., B–N coordinated triaryl pyrazole: effect of dimerization, and optical and NLO properties. *J. Mater. Chem. C* **2019**, *7* (40), 12725-12737.
46. Kinastowska, K.; Piela, K.; Gordel, M.; Żak, A.; Kołkowski, R.; Samoć, M., Gold nanoparticle-decorated graphene as a nonlinear optical material in the visible and near-infrared spectral range. *Phys. Chem. Chem. Phys.* **2018**, *20* (27), 18862-18872.
47. Ekbote, A.; Patil, P. S.; Maidur, S. R.; Chia, T. S.; Quah, C. K., Structural, third-order optical nonlinearities and figures of merit of (E)-1-(3-substituted phenyl)-3-(4-fluorophenyl) prop-2-en-1-one under CW regime: New chalcone derivatives for optical limiting applications. *Dyes Pigm.* **2017**, *139*, 720-729.

48. Liu, F.; Marongiu, D.; Pau, R.; Sarritzu, V.; Wang, Q.; Lai, S.; Lehmann, A. G.; Quochi, F.; Saba, M.; Mura, A.; Bongiovanni, G.; Mattoni, A.; Caddeo, C.; Bosin, A.; Filippetti, A., Ag/In lead-free double perovskites. *EcoMat* **2020**, 2 (1), e12017.
49. Pan, L.; Tamai, N.; Kamada, K.; Deki, S., Nonlinear optical properties of thiol-capped CdTe quantum dots in nonresonant region. *Appl. Phys. Lett.* **2007**, 91 (5), 051902.
50. Ultrafast optical nonlinearity of blue-emitting perovskite nanocrystals. *Photonics Res.* **2018**, 6 (6), 554-559.
51. Wang, Y.; Yang, X.; He, T. C.; Gao, Y.; Demir, H. V.; Sun, X. W.; Sun, H. D., Near resonant and nonresonant third-order optical nonlinearities of colloidal InP/ZnS quantum dots. *Appl. Phys. Lett.* **2013**, 102 (2), 021917.
52. Z-scan measurement of the nonlinear refractive index of monolayer WS₂. *Opt. Express* **2015**, 23 (12), 15616-15623.
53. Bulutay, C.; Turgut, C. M.; Zakhleniuk, N. A., Carrier-induced refractive index change and optical absorption in wurtzite InN and GaN: Full-band approach. *Phys. Rev. B* **2010**, 81 (15), 155206.
54. Broadband femtosecond nonlinear optical properties of CsPbBr₃ perovskite nanocrystals. *Opt. Lett.* **2018**, 43 (3), 603-606.
55. Han, Q.; Wu, W.; Liu, W.; Yang, Q.; Yang, Y., Two-photon absorption and upconversion luminescence of colloidal CsPbX₃ quantum dots. *Opt. Mater.* **2018**, 75, 880-886.
56. Zou, S.; Yang, G.; Yang, T.; Zhao, D.; Gan, Z.; Chen, W.; Zhong, H.; Wen, X.; Jia, B.; Zou, B., Template-Free Synthesis of High-Yield Fe-Doped Cesium Lead Halide Perovskite Ultralong Microwires with Enhanced Two-Photon Absorption. *J. Phys. Chem. Lett.* **2018**, 9 (17), 4878-4885.

57. Chen, W.; Zhang, S.; Zhou, M.; Zhao, T.; Qin, X.; Liu, X.; Liu, M.; Duan, P., Two-Photon Absorption-Based Upconverted Circularly Polarized Luminescence Generated in Chiral Perovskite Nanocrystals. *J. Phys. Chem. Lett.* **2019**, *10* (12), 3290-3295.
58. Walters, G.; Sutherland, B. R.; Hoogland, S.; Shi, D.; Comin, R.; Sellan, D. P.; Bakr, O. M.; Sargent, E. H., Two-Photon Absorption in Organometallic Bromide Perovskites. *ACS Nano* **2015**, *9* (9), 9340-9346.
59. Carrier dynamics and optical nonlinearity of alloyed CdSeTe quantum dots in glass matrix. *Opt. Mater. Express* **2017**, *7* (5), 1547-1556.
60. Lad, A. D.; Kiran, P. P.; More, D.; Kumar, G. R.; Mahamuni, S., Two-photon absorption in ZnSe and ZnSe/ZnS core/shell quantum structures. *Appl. Phys. Lett.* **2008**, *92* (4), 043126.
61. Mary, K. A. A.; Unnikrishnan, N. V.; Philip, R., Role of surface states and defects in the ultrafast nonlinear optical properties of CuS quantum dots. *APL Mater.* **2014**, *2* (7), 076104.
62. Determination of bound-electronic and free-carrier nonlinearities in ZnSe, GaAs, CdTe, and ZnTe. *J. Opt. Soc. Am. B* **1992**, *9* (3), 405-414.
63. Van Stryland, E. W.; Vanherzeele, H.; Woodall, M. A.; Soileau, M.; Smirl, A. L.; Guha, S.; Boggess, T. F., Two photon absorption, nonlinear refraction, and optical limiting in semiconductors. *Opt. Eng.* **1985**, *24* (4), 244613.
64. Gu, B.; Fan, Y.-X.; Chen, J.; Wang, H.-T.; He, J.; Ji, W., Z-scan theory of two-photon absorption saturation and experimental evidence. *J. Appl. Phys.* **2007**, *102* (8), 083101.

Supporting Information

Third-Order Nonlinear Optical Properties and Saturation of Two-Photon Absorption in Lead-Free Double Perovskite Nanocrystals under Femtosecond Excitation

Aamir Mushtaq^{§#}, Bapi Pradhan^{§#}, Dushyant Kushavah[§], Yiyue Zhang[§], Mathias Wolf[§],
Nadine Schrenker^α, Eduard Fron[§], Sara Bals^α, Johan Hofkens^{§,δ} Elke Debroye[§], Suman
Kalyan Pal^{§*}

[§]*School of Basic Sciences and Advanced Material Research Center, Indian Institute of
Technology Mandi, Kamand 175005, H.P, India*

[§]Department of Chemistry, KU Leuven, Celestijnenlaan 200F, 3001 Heverlee, Belgium

^δMax Planck Institute for Polymer Research, Ackermannweg 10, 55128 Mainz, Germany

^αElectron Microscopy for Materials Research, University of Antwerp, Groenenborgerlaan,
171, 2020 Antwerp, Belgium

Material Synthesis

Chemicals

BiCl₃ (99%, Sigma), InCl₃ (99%, Sigma), CsCl (99.99%, Alfa Aesar), AgCl (99.99%, Alfa Aesar), oleic acid (90%, Sigma), isopropanol (Merck), dimethyl sulfoxide (DMSO, >99%, Sigma) were purchased and used as-is without any further purification. All the salts were stored under N₂ atmosphere to prevent from moisture and oxygen attack.

Synthesis of Cs₂AgIn_{0.9}Bi_{0.1}Cl₆ nanocrystals (NCs)

A stoichiometric ratio of salts was taken in a glass vial and dissolved in DMSO to form the precursor solution.¹ 0.2 mmol CsCl (33.7 mg), 0.1 mmol AgCl (14.3 mg), 0.01 mmol BiCl₃ (3.15 mg) and 0.09 mmol InCl₃ (19.9 mg) were dissolved in 5 mL DMSO by prolonged stirring. 100 μ L precursor solution was swiftly injected into the 5 mL isopropanol under vigorous stirring. After that, the solution was centrifuged at 5000 rpm for 3-5 mins to discard the large crystals. The as-obtained colloidal solution was used for further characterization and nonlinear optical studies.

Experimental details

The absorption spectrum of the NCs was recorded using a Shimadzu UV-2700 instrument. Steady state photoluminescence (PL) was recorded in an Edinburgh FLS980 spectrometer at 260 nm excitation with an acquisition time of 0.1 seconds. The PL lifetime measurement was performed using laser pulses generated by a system consisting of a Nd:YAG laser (Quanta-Ray INDI-40, Spectra Physics) and an optical parametric oscillator (OPO) (355 nm, 406 nm and 488 nm wavelengths). The pulse duration was estimated to be 8 ns while the time resolution of the experiment was about 10 ns. The excitation light was focused on the sample by a lens ($f \sim 300$ mm). A small part of the excitation light was sent to a fast photodiode to generate a trigger signal. After excitation, emission signals were collected in a right-angle configuration. Emission signals were collected, filtered and focused on the entrance slit of a 30 cm focal length spectrograph. The emitted light was dispersed by a computer-controlled spectrograph SpectroPro-300i Acton Research. A photomultiplier tube (PMT) (Hamamatsu, R928) was used as detector and the transient electrical signal was displayed by an oscilloscope connected to the control computer. A homemade LabVIEW based software was used to control and trigger the instruments, read, average and store the transient data. Tecnai G2 F20 instrument, FEI Co., USA, was used for capturing transmission electron microscopy (TEM) images. Scanning electron microscopy (FEI FE-SEM Nova NanoSem 450 instruments) was used to approximate

the average thickness of film. Two-photon fluorescence measurements were carried out using an inverted optical microscope (Ti-U, Nikon) equipped with a piezoelectric stage (P517.3CL, Physik Instrumente). The sample was excited using 800 nm pulsed laser irradiation (Mai Tai HP, Spectra-Physics, 120 fs, 80 MHz). The beam was focused using an objective lens (Nikon, 60x Plan Apo, air, NA 0.95). The signal was collected through the same objective lens. Spectra were recorded at different intensities using a charge-coupled device (CCD) camera (DU920P, Andor) with a spectrograph (iHR320, Horiba) and Labspec software (Horiba). The integration time for each spectrum was 25 seconds. In order to block excitation light, a 750 short-pass (ET750sp, Chroma) filter was used. Out of focus signal was removed by a pinhole (diameter 100 μm).

Before starting the measurements, it is prerequisite to measure the known sample to validate the configuration of a Z-scan setup. We have performed open-aperture (OA) Z-scan on carbon disulphide (CS_2) at 800 nm. Fitting of the OA curve yielded a value of nonlinear absorption coefficient of 0.08 mm/GW which is very close to that (0.06 mm/GW) reported earlier using a laser source of 50 fs pulse width and 1 kHz repetition rate.²

High-resolution high-angle annular dark-field scanning transmission electron microscopy (HAADF-STEM) images were acquired in a probe-corrected cubed FEI Titan microscope operating at 300 kV. EDX-based elemental maps were recorded using Super-X detector.

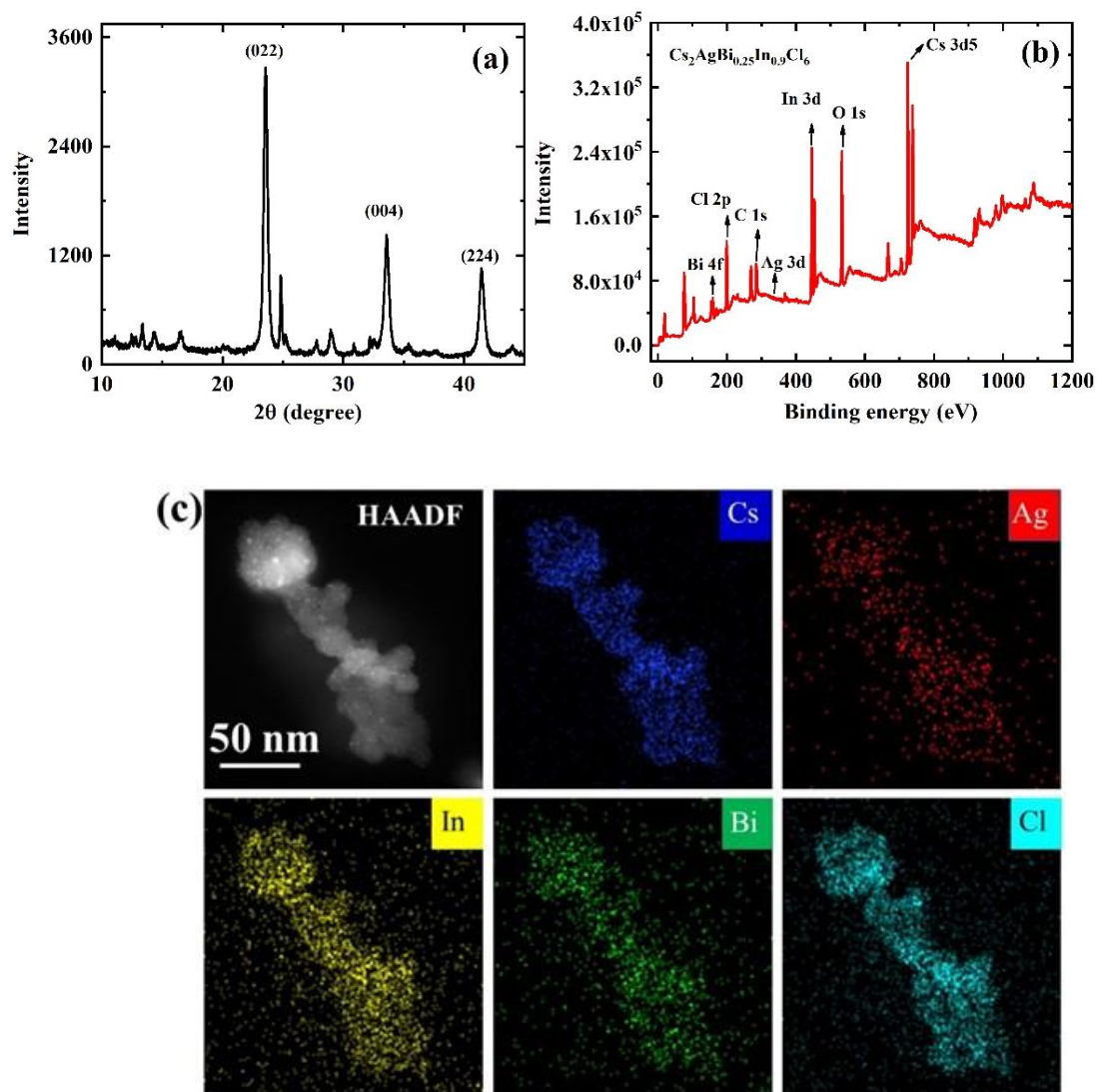


Figure S1. (a) XRD pattern, (b) XPS spectrum of double perovskite nanocrystals (NCs) and (c) High-angle angular dark-field image (HAADF) image of double perovskite NCs and corresponding EDX elemental maps of Cs, Ag, In, Bi, and Cl.

Table S1. Elemental distribution of NCs from the EDX measurements

Z	Element	Family	Atomic Fraction (%)	Atomic Error (%)	Mass Fraction (%)	Mass Error (%)	Fitting error (%)
17	Cl	K	57.40	4.77	27.81	1.56	1.27
47	Ag	K	9.43	1.56	13.90	2.13	7.11
49	In	L	10.38	1.45	16.29	2.04	0.83
55	Cs	L	22.23	3.01	40.39	4.87	0.36
83	Bi	M	0.56	0.09	1.61	0.25	4.41

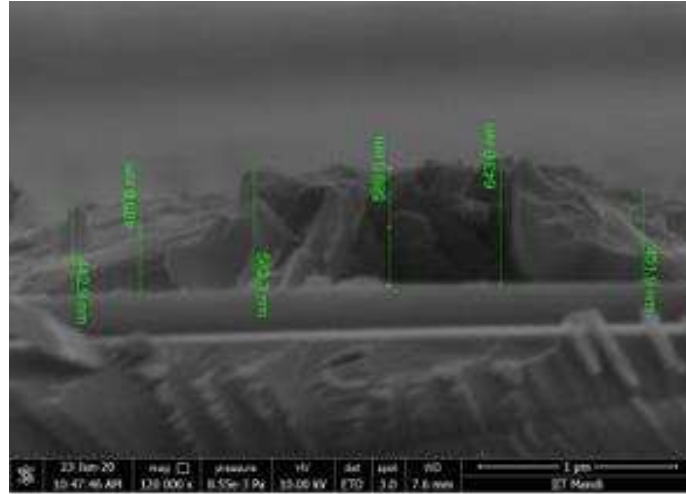


Figure S2. SEM image of a dropcasted sample of NCs. The average thickness in the region of the incident laser beam for Z-scan measurements was calculated to be 512 nm.

Correction of PL spectrum

The following relation was used

$$S_c = (S - S_0) * M_{\text{Correct}}$$

Where,

S_c : zero and response corrected emission signal

S : measured emission signal

S_0 : emission detector zero count

M_{Correct} : wavelength dependent emission correction factor

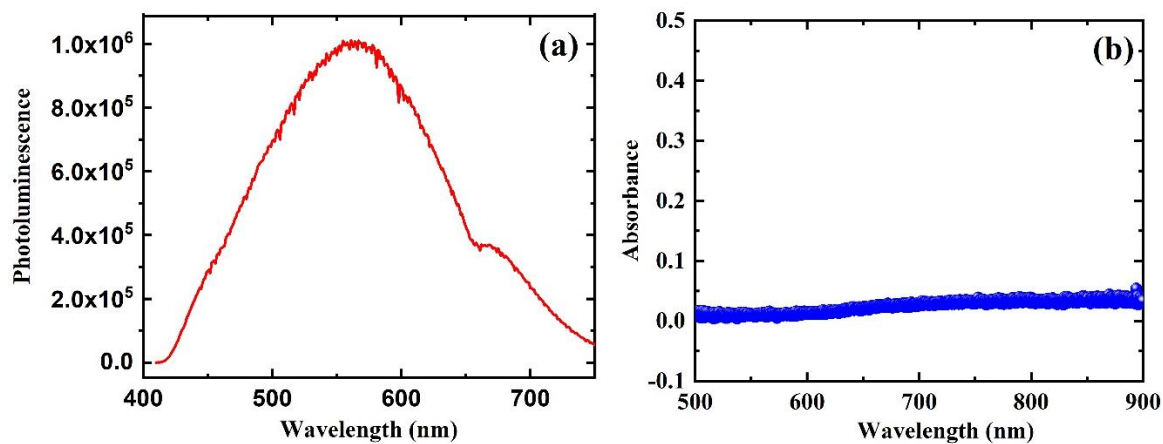


Figure S3: (a) Uncorrected PL spectrum of the NCs. (b) Absorption spectrum of the double perovskite NC film.

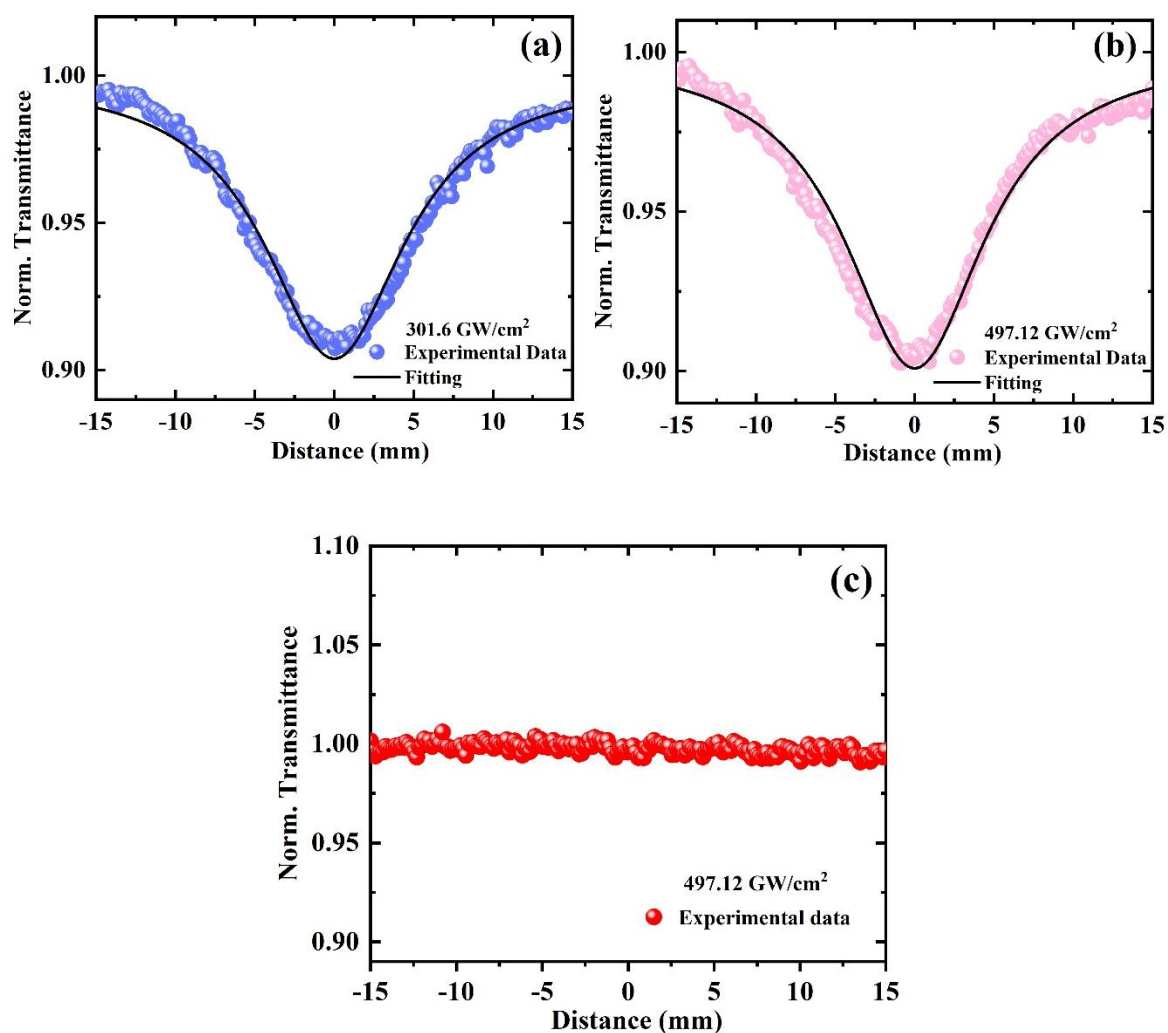


Figure S4. OA Z-scan curves at (a) intermediate and (b) high intensities recorded for NC films. (c) OA Z-scan curve of the cover slip at the highest intensity used in the experiment.

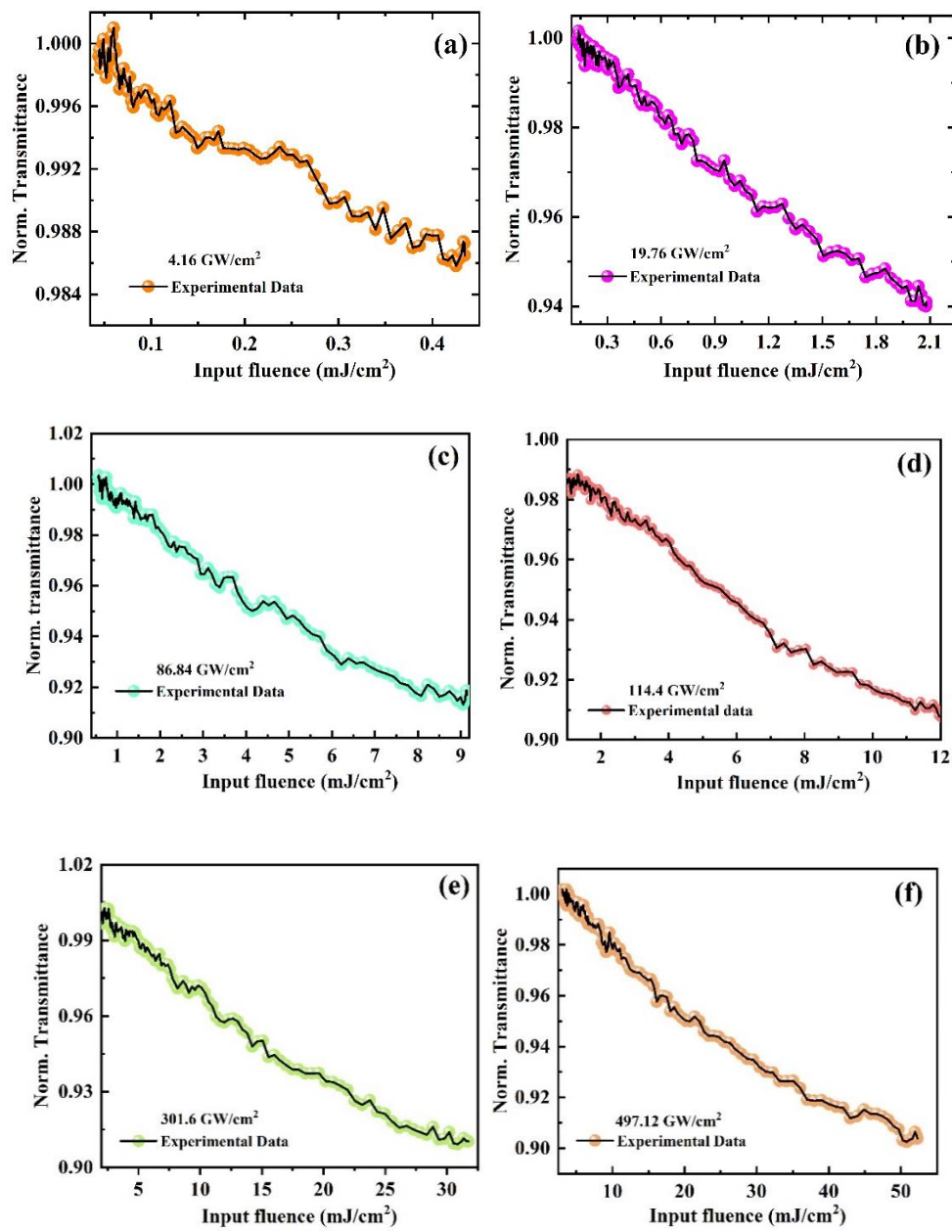


Figure S5. Optical limiting curves at each respective intensity.

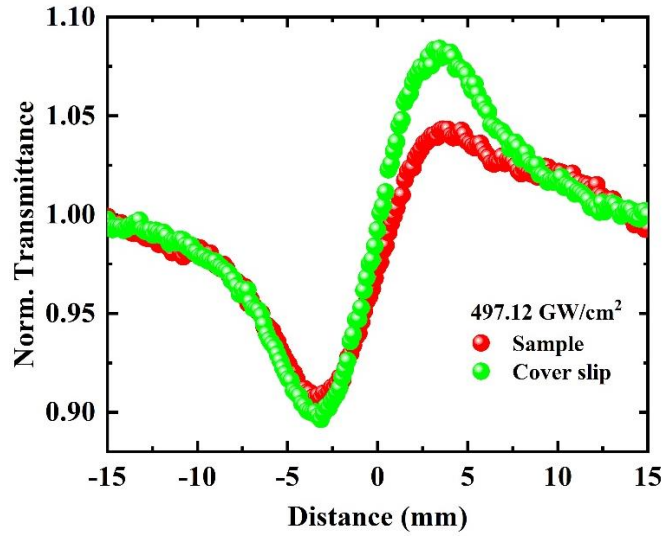


Figure S6. Comparison of CA Z-scan curves of the cover slip and NCs.

Concentration of NCs

The concentration (N) is calculated from the volume of NCs in one cc.³

$$N = \frac{1}{\frac{4}{3} \times 3.14 \times (1.65 \text{ nm})^3} = 5.3171 \times 10^{19} \text{ cm}^{-3}$$

This is an approximate calculation based on the assumption that NCs are densely packed.

Actual value of concentration will be much lower than the value mentioned here which means actual value of σ_{TPA} could be much higher than the estimated one.

The two-photon absorption cross-section was calculated as

$$\sigma_{TPA} = \frac{(h\nu)}{N} \beta = \frac{2.482 \times 10^{-19} \text{ J} \times 21.90 \frac{\text{cm}}{\text{GW}}}{5.317 \times 10^{19} \text{ cm}^{-3}} = 10.22 \times 10^{-47} \text{ cm}^4 \text{ s} = 1.022 \times 10^4 \text{ GM}$$

References

1. Yang, B.; Mao, X.; Hong, F.; Meng, W.; Tang, Y.; Xia, X.; Yang, S.; Deng, W.; Han, K., Lead-Free Direct Band Gap Double-Perovskite Nanocrystals with Bright Dual-Color Emission. *J. Am. Chem. Soc.* **2018**, *140* (49), 17001-17006.
2. Mixed two- and three-photon absorption in bulk rutile (TiO₂) around 800 nm. *Opt. Express* **2012**, *20* (3), 3118-3128.
3. Krishnakanth, K. N.; Seth, S.; Samanta, A.; Venugopal Rao, S., Broadband ultrafast nonlinear optical studies revealing exciting multi-photon absorption coefficients in phase pure zero-dimensional Cs₄PbBr₆ perovskite films. *Nanoscale* **2019**, *11* (3), 945-954.